Compact Nanosecond Magnetic Pulse Compression Generator for High-Pressure Diffuse Plasma Generation

M.D.G. Evans*, V.J.P. Baillard*, P.D.G. Maqueo, J.M. Bergthorson, S. Coulombe

***Abstract*— We report on the development of a low-cost, adjustable high-voltage/high-power nanosecond pulse generator for diffuse plasma generation in a high-pressure gas-discharge cell. The generator produces scalable impulsions of 0 to 40 kV, at an adjustable pulse repetition frequency up to 7 kHz. Details pertaining to its working principles, electrical architecture, components, and specifications are presented. Voltage and current pulses are measured for resistive loads of 1.5 kΩ to 5 MΩ. The energy per pulse along with the generator's overall efficiency are presented as a function of the input voltage. A maximum value of 13.5 mJ/pulse can be delivered to a 3 kΩ load. Our preliminary investigation using a pin-to-plate geometry in air and at pressures up to 2.75 atm [280.5 kPa] demonstrates the production of uniform diffuse plasma volumes. The domain of existence of the diffuse plasma regime is briefly explored, as a function of pressure and voltage pulse amplitude.**

***Index Terms*— Plasmas, Plasma generation, Plasma devices, Pulse compression circuits, Pulse Generation, Pulse power systems**

I. Introduction

Over the last decade, several researchers of the plasma processing community have dedicated considerable effort to the generation of diffuse non-equilibrium plasmas, free of filaments and localized hot spots, at atmospheric pressure. So far, the most promising way of producing such plasmas is through the use of short-duration, repetitive, high-voltage pulses (1 ns – 1 µs), as opposed to conventional high-voltage DC or AC sources. Short pulses ensure precise and timed deposition of energy to the plasma load in a uniform and repetitive manner. Short pulses enhance electron impact chemistry [1], and increase the permissible voltage limit that may be attained prior to spark channel formation [2], thereby minimizing gas temperature increase [3]. Several fields of application, such as plasma-assisted combustion (PAC) [4][5], plasma-assisted ignition (PAI) [6][7], fuel reforming [8], and plasma medicine [9][10], now make use of this technology.

High-voltage drift-step recovery diodes (DSRD) [11][12] and semiconductor opening switches (SOS) [13][14] are the main current contender technologies for high-voltage, short-pulse generation. Unfortunately, the limited availability and high cost of these opening switches remain problematic for industrial generator development. Pulse generation using commercially-available ultra-short recovery time diodes has yielded similar results to the DRSD and SOS technology [15], but limited hold-off voltage and frequent failure of the diodes have been reported for high pulse-repetition frequencies [16].

Magnetic pulse compression (MPC) technology offers the possibility of constructing robust high-voltage pulse generators using few components prone to failure. This technology delivers higher energy per pulse, longer pulse width, but with lower pulse repetition frequency compared to DSRD and SOS technologies. MPC relies on the use of capacitors and variable inductors, wound on amorphous ferromagnetic cores in a toroidal shape, to store energy and release it in successive voltage step-up transformations over progressively shorter periods of time [17]. The variable inductors are wound toroids, used as magnetic switches. Their impedance alternates between low and high values depending on the magnetic flux-swing in their core, induced by the current in their windings. MPC is usually combined with relatively slow solid-state switches (thyristors, SCRs, or IGBTs), which modulate the power delivery of an initial energy storage device such as a capacitor or a power supply. Many MPC cell architectures are possible, ranging from parallel and series compression, to combinations including Marx banks. Many of these architectures produce pre-pulse waveforms, and have limited repetition rates around 1-2 kHz [18][19][20].

In this article, we report on the development of a low-cost compact magnetic pulse compressor, free of reset circuits, using a novel parallel, synchronized branch system in the pulse compression circuit used to increase the efficiency of the output transformer. First, the circuit architecture and its components are presented. Then, the generator's operation on a full cycle is presented for a 3 kΩ load, along with its performance with a range of different resistive loads. Finally, diffuse air plasma volumes are generated in a pin-to-plate geometry up to 2.75 atm [280.5 kPa], and the domain of existence and energy deposition is mapped as a function of gas pressure and pulse amplitude.

II. Experimental Setup

A. Functional Architecture of the Generator

Fig. 1 shows the general block diagram of the MPC generator. The DC Power Block provides the required amount of energy necessary for the entire MPC generator, which is stored in the Primary Pulse Block at the start of each cycle. The Transistor-Transistor Logic (TTL) Trigger Generator's signal is fed to the Control Block, which drives the Primary Pulse Block to release energy in the form of a high-current pulse. This energy is then cascaded to the Magnetic Pulse

Compression Block, where the pulse duration is significantly reduced. The output of the Magnetic Pulse Compression Block is fed to the Load of choice, which may be a resistor or a gas discharge cell.

B. Trigger & Control Block Circuit

Fig. 2 shows the equivalent Control Block Circuit. A TTL signal (5 V, Δt = 6.2 µs) is sent out from the external trigger generator (*Berkeley Nucleonics*, BNC 565) to amplifier *A* (*MICROCHIP*, TC4420), which provides the adequate level of power to drive the parallel optocoupler bank O_1-O_6 (*Vishay Semiconductors*, VO3120). Resistors R_{O1}-R_{O6} (100 Ω) ensure that each optocoupler receives an equal and controlled current. Each optocoupler provides isolation for the TTL Trigger Generator from reflected power in the Primary Pulse Block, which could otherwise spuriously trigger a conventional parallel bank of amplifiers in its place. Capacitor C_{A1} (4.7 µF) stabilizes power supply V_A, set to 10 V, and capacitor C_{A2} (2.5 nF) stabilizes the output of *A*. The power supply V_O, set to 30 V, powers the bank of optocouplers, while capacitors C_{O1}-C_{O6} (0.1 µF each) stabilize the supply voltage for each optocoupler. The output of each optocoupler is connected in series to a resistor R_{G1}-R_{G6} (100 Ω each) and to the gate of the paired transistor in the Primary Pulse Block. The optocoupler signals are identified as S_1-S_6. R_{G1}-R_{G6} stabilize the operation of each transistor, protect the optocouplers, and control the rise time of the control signal applied to each transistor.

C. Primary Pulse Block & Magnetic Pulse Compression Block

Fig. 3 shows the architecture of the Primary Pulse Block and the Magnetic Pulse Compression Block. Selected circuit nodes (N_0-N_6) are identified on the figure, and will be used as measurement references in Section 2. The magnet wire used throughout this project for the windings around ferromagnetic materials is 18 AWG (*Rea Magnet Wire Company*, Pulse Shield), and the transformer's winding ratios will be expressed in full numbers of turns (N_{pri}:N_{sec}).

PS is an adjustable DC power supply (*Sorensen*, DCR 600-4.5B), and is also referred to as the DC Power Block. C_0 (10 µF) and C_1 (3.7 µF) are polypropylene capacitors, and inductor L_0 (560 µH) is used as a high-current choke made with 100 turns of 18 AWG magnet wire wrapped around a ferrite core (*Eaglerise Electric & Electronic*). Diode D_0 is a high-current diode (*Fairchild Semiconductor*, RURG80100), with 1 kV of hold-off voltage. Transistor bank T_1-T_6 is composed of IGBTs (*IXYS*, IXYH60N90C3), with 900 V of hold-off voltage, and controlled with signals S_1-S_6. Pulse transformer PT_1 is made of a stack of 4 nanocrystalline cores (*Hitachi Metals*, FT3KM F6045G, B_{sat} = 1.23 T, $\mu_{r,max} \simeq 70000$), with 1:50 step-up ratio, and may be considered as the junction point between the Primary Pulse Block and the Magnetic Pulse Compression Block. Capacitor C_2 (1.1 nF) is made of two ceramic capacitors in series.

Pulse transformer PT_2 is made of a stack of 4 nanocrystalline cores (*Hitachi Metals*, FT3KM F4535G, B_{sat} = 1.23 T, $\mu_{r,max} \simeq 70000$), with 7.5:12 step-up ratio. C_3 (500 pF) is a ceramic disc capacitor. Magnetic switch MS_1 is made of two 3-core stacks in series (*Hitachi Metals*, MP3210M4AS, B_{sat} = 0.57 T). Each 3-core stack is wrapped with two parallel branches of 20 turns each winded in the same direction so that the coercive currents add up to generate the magnetic flux. Magnetic switch MS_2 is made of a single 3-core stack of the same material as MS_1 using the same parallel winding configuration. C_{4a} and C_{4b} (470 pF) and C_{5a} and C_{5b} (235 pF) are ceramic disk capacitors. Pulse transformers PT_{3a} and PT_{3b} are each made of a single core of the same material as MS_1 and MS_2, with a 10:33 step-up ratio. Internal stabilizing resistor R_S (5 MΩ) is a metal oxide resistor, and the load resistor R_L is placed externally to the generator. PT_{3a}, PT_{3b}, and R_S are immersed in an oil bath to prevent gas breakdown, between the primary and secondary windings of PT_{3a} and PT_{3b}, through the core material. The entire generator, excluding *PS* and the trigger generator, has a volume of under 0.02 m^3. The total cost of the generator, including an encasement and cooling fans, is under 1000 USD.

D. Electrical Diagnostics

Voltage measurements in the Control Block Circuit were made using a 10X passive probe (*Tektronix*, P2200, 10 MΩ, 16 pF). Voltages measured in the Primary Pulse Block were made with a second 10X passive probe (*Tektronix*, P6016A, 10 MΩ, 13 pF), and those in the Magnetic Pulse Compression Block were made using 1000X passive voltage probes (*Tektronix*, P6015A, 100 MΩ, 3 pF). Currents were measured using two types of Rogowski coils (*Pearson Electronics*, Model 411 & Model 110A) for resistive load operation and plasma generation, respectively. All electrical measurements were recorded using a digital oscilloscope (*Tektronix*, TDS-3054B).

E. Gas Discharge Cell

Fig. 4 shows the gas discharge cell used for the generation of diffuse plasma under high-pressure conditions. The body of the gas discharge cell is made of a four-way cross (*Kurt J. Lesker* Company, QF40-150-X). Compressed air is fed to the reactor through the inlet, and the pressure in the chamber is regulated by a needle valve placed at the exit of the reactor. The pressure in the discharge cell is monitored by a pressure gauge, and the maximum permissible pressure differential is 26 psig (corresponding to a maximum total pressure of 2.75 atm [279 kPa]). The positive terminal of the generator is connected to a pin anode using a high-voltage feedthrough with 25 kV DC rating. The negative terminal of the generator is connected to a grounded plane cathode mounted on the flanged cap. The inter-electrode distance is 1.4 cm, and the capacitance of the discharge cell electrodes, including the high-voltage cable, was measured to be 10.4 pF.

III. RESULTS & DISCUSSION

A. Operation & Energy Cascade Through the MPC Generator

The operation of the pulse generator is described at a pulse repetition frequency, ν, of 1 kHz, a charging voltage set point, V_{PS}, of 200 V, and an external resistive load, R_L, of 3 kΩ. Fig. 5 shows the operation of the Control Block along with the Primary Pulse Block. The nodes previously identified in Fig. 3 are referenced hereafter.

The Control Block circuit produces a square pulse of 30 V (Δt = 6.2 µs) applied to each of the S_1-S_6 gates, which actions the transistor bank, and fully discharges C_1 through D_0, S_1-S_6, and the primary winding of PT_1. It should be noted that PS and C_0 charge C_1, through L_0, during the transistor off-time, and minimally discharge during the transistor's on-time, due to L_0's high inductance value. This can be seen in Fig. 5 (left) where the total current through the IGBT stack reaches a value of 190 A in an almost perfect half-sinusoid. This energy charges C_2 through PT_1. Here, D_0 hinders the back current of this resonant transfer, which may damage the IGBT stack. In Fig. 5 (left) a slight reverse current can be observed in I_{IGBT}, which is due to the reverse recovery time of 200 ns for D_0. Fig. 5 (right) shows the voltages at nodes N_0, N_1, and $N_{1'}$, respectively. Once the IGBT stack is conducting, the voltages at nodes N_1 and $N_{1'}$ collapse, and the voltage at N_0 remains constant, thus demonstrating the stability provided to V_{PS} with L_0 and C_0. Voltage $V_{N1'}$ is the voltage across the primary windings of PT_1, which rings down to the opposite polarity of the charging voltage and transforms the 190 A peak-current pulse into an equal duration voltage signal across C_2, up to 10 kV, as seen on Fig. 6 (right). It should also be noted that a fraction of C_1's charge remains on the capacitor at approximately 8 µs.

Fig. 6 (left) shows as a reference the current through the transistor stack (I_{IGBT}), as well as the current through the primary ($I_{PT2\text{-}PRI}$) and secondary windings ($I_{PT2\text{-}SEC}$) of PT_2. I_{IGBT} is shown again with the solid black line while $I_{PT2\text{-}PRI}$ and $I_{PT2\text{-}SEC}$, are shown with the dashed and dot-dashed lines respectively. Fig. 6 (right) shows the voltages at nodes N_2, $N_{2'}$, and N_3 with the solid, dashed and dot-dashed line styles, respectively. As I_{IGBT} is flowing, capacitor C_2 charges with current $I_{PT2\text{-}PRI}$ reaching a maximum value of -4 A. Before MS_1 saturates, C_2 has fully charged up to its maximum voltage of -10.5 kV, as illustrated by trace V_{N2a}, and then discharges through the primary windings of PT_2, with a current of over 27 A with a duration of ~1 µs. The voltage across the secondary windings of PT_2, illustrated by $V_{N2'}$, is stepped up by PT_2 and charges C_3, shown with V_{N3}, up to a voltage of 10 kV. The visible increase in V_{N3} from 0 to 2.5 µs, corresponds to the time during which PT_2 has not yet saturated, and part of the energy stored in C_1 is transferred to C_3. Despite the loss, this energy is used to reverse the direction of PT_2's magnetic flux, which enhances the main charge transfer, up to 10 kV, occurring from 7 to 8 µs. The negative value in $I_{PT2\text{-}SEC}$ that occurs at 8 µs results from MS_1 saturating.

Fig. 7 (left) shows the voltages at circuit nodes N_{4a}, N_{4b}, N_{5a}, and N_{5b}. Fig. 7 (right) shows the voltage at node N_6, corresponding to the generator's output. Once C_3 has charged up to 10 kV, magnetic switch MS_1 saturates, as indicated by the steep fall time of V_{N3} at 7.8 µs on Fig. 6 (right), and cascades the energy stored in C_3 through two parallel branches (a & b). Capacitors C_{4a} and C_{4b} are then charged up to 6.8 kV, where they store this energy for 500 ns, in a similar manner, until magnetic switch MS_2 saturates and cascades the energy to C_{5a} and C_{5b} over 150 ns. These voltages, which are also the voltages at the primaries of PT_{3a} and PT_{3b}, are individually stepped up and added to create the final output voltage pulse with amplitude 29 kV, and full width at half maximum (FWHM) of 90 ns.

B. Noteworthy Design Considerations

Impedance matching, from stage-to-stage inside the generator, was applied to obtain the same effective capacitance with the relation $C_n = (N_{n+1}/N_n)^2 C_{n+1}$ [21]. Due to the non-ideal efficiency of the pulse transformers and magnetic switches, either the upstream capacitor value was increased, or the downstream one decreased, from the prescribed values to accommodate for this.

During the MPC cycle, PT_1 never fully saturates. Its partial saturation is driven by PT_2's saturation, which is driven by MS_1's saturation. Therefore, only a fraction of the energy stored in C_1 is used to reverse the direction of the magnetic flux in PT_1, as can be seen on Fig. 6 (right). This is a possible explanation for the remaining charge on C_1, as seen in Fig. 5 (right).

The observed holding-time of ~500 ns on C_4 arises from minimizing the leakage inductance of MS_2 by covering its entire magnetic material volume with the parallel branch configuration. Also, the use of parallel branches focuses on the maximization of the step-up efficiency of $PT_{3\{a,b\}}$. A maximum number of turns on both the primary and secondary produce a fast switching time and high voltage step-up ratio. It should be noted that a fixed number of turns on the primary would yield a holding time equal to that of MS_2's switching time for an optimized output. Consequently, the parallel branch inductors MS_1 and MS_2 were synchronized to drive equal amounts of power in a more robust manner.

As a final design consideration, the maximum attainable pulse repetition rate, ν_{max}, is a function of the available power from *PS*, and the efficiency loss with increased temperature of the transistor bank and magnetic cores. The quality and performance of the magnetic switching may degrade with increased frequency due to the decrease in the magnetic material's permeability and an increase in impedance. Here, ν_{max}, was limited to ~7 kHz for the present generator, as *PS* was the limiting factor.

C. Resistive Load Operation

Fig. 8 shows the output of the pulse generator into various resistive loads. It should be noted that the external load of 5 MΩ consists of the circuit with only the internal stabilizing resistor R_S. Since only the output of the pulse generator is analyzed in this section, the new time scale reference will be the time at which the rising edge of the output voltage reaches a value of 1 kV. As the load impedance increases, the output voltage signal transits from a unipolar pulse to a bipolar pulse. This effect is more readily observable for higher load impedances where higher charging voltages are used. The bipolar nature of the pulse occurs, for increasing load impedances, as PT_{3a} and PT_{3b} saturate when no more current can be passed through the load. At this point, there is only a LC circuit made up of the series windings of PT_{3a} and PT_{3b}, which short-circuit the generator's output prompting LC resonance, as occurs in an open-secondary transformer output. If larger cores of this magnetic material were available, fewer windings would be required to reach the desired voltage at the output, decreasing both the capacitance and inductance of the LC circuit. The output voltage can be controlled by varying the input voltage of *PS*, as seen in Fig. 8.

Fig. 9 shows the peak voltage (left), V_p, and pulse duration at FWHM (right), τ_{FWHM}, of the generator's output signal for all external loads tested at different charging voltages. The values of V_p and τ_{FWHM} for R_L = 5 MΩ are used to identify the final point of the trend in the effect of the load on the generator's output. It should be noted that no voltage measurements for R_L = 5 MΩ and V_{PS} = 210 V were performed as the generator's output would exceed the voltage rating of the P6015A probe. V_p increases to the final value of the open circuit until no more potential may be created. τ_{FWHM} increases as a function of the increasing load, with the highest values occurring for the lowest charging voltages. As the charging voltage increases, the pulse width decreases due to shorter switching times and holding times of the magnetic switches caused by a greater discharge current of I_{IGBT} over the same time. The rise time is linked to the saturation of MS_2, while the fall time is produced by the saturation of $PT_{3\{a,b\}}$. It may be observed that τ_{FWHM} is almost constant for R_L = 3 kΩ. The spread of τ_{FWHM} for a fixed load impedance increases as the load deviates from the 3 kΩ point, indicating that the generator's output is matched for this load.

D. Energy Deposition

Fig. 10 shows the instantaneous power delivered to the load (left) and cumulative energy deposition (right), both for an external resistive load of 3 kΩ. The maximum instantaneous peak power obtained is 220 kW, and the maximum energy delivered per pulse is 13.5 mJ.

Fig. 11 shows the energy deposited per pulse of the generator for all the resistive loads and voltage set points of voltage source *PS*. The energy per pulse is calculated with (1).

$$E_{pulse} = \int_{t_1}^{t_2} V(t) I(t)\, dt \tag{1}$$

The maximum attainable power output of the generator occurs for a load impedance of 3 kΩ, further indicating the matched output impedance of the generator ranging around this value. As the load impedance increases, the coupled energy diminishes since a bipolar signal is produced at the output of the generator, with the negative polarity pulse short-circuited to the ground.

E. Diffuse Plasma Generation

As touched upon in the introduction, PAC and PAI are promising applications of processing plasmas, promoting a more complete and efficient combustion process [22][23]. These technologies are being researched to reduce the formation of harmful pollutants such as NO_x, SO_x, and CO commonly produced by flames [24]. Despite the majority of combustion reactions taking place at atmospheric pressure and above, most of the research on PAC has focused on low-pressure conditions (25-300 Torr [3.3-40 kPa]) for the aerospace industry [25][26]. PAC at atmospheric pressure has mainly focused on the use of nanosecond pulsed spark discharges to thermally stabilize flames, and extend their lean flammability limit [27][28]. Spark discharges increase the translational temperature of atmospheric-pressure air by several thousands of Kelvin [29], and increase the production of NO when applied to combustion enhancement [30]. Recent work has made use of diffuse plasmas at atmospheric pressure to increase the blow-off velocity of laminar premixed flames [31], and to activate the unburned fuel stream of diffusion flames [32]. For the successful implementation of PAC in high-pressure environments, such as gas turbines, a sufficient pool of radicals must be generated while avoiding the temperature increase brought on by the spark discharge.

In this work, diffuse plasma volumes were produced using the MPC generator. The external resistive load, R_L, was replaced with the gas discharge cell, as presented in Fig. 4. The discharge cell was initially filled with extra-dry compressed air to a prescribed initial pressure (0, 4, or 8 psig [101, 128, or 156 kPa]) and then sealed off. For each of these pressure settings, the peak voltage of the pulse generator was gradually increased to reach the maximum permissible value for the diffuse plasma regime, avoiding the transition to a spark discharge. As expected, the peak voltage required for spark formation increased, as pressure increased in the gas discharge cell. These voltage levels are defined as V_{p1}, V_{p2}, and V_{p3}. Once the peak voltage was reached, the pressure was gradually increased in increments of 2 psi (13.8 kPa) until extinction of the plasma, as verified with digital photography, with an exposure time of 2 s. Fig. 12 shows a series of digital images illustrating the appearance of the diffuse plasma generated in air for a pulse repetition frequency of 1 kHz.

This data show a decaying energy input per pulse as a function of the cell pressure. This trend is to be expected with an increased number of collisions and recombination reactions occurring per unit time. Although the generation of diffuse plasma through the application of pulsed power can be heavily device-specific (electrode material and geometry, pulse rise-time, duration, and frequency, etc.), these results are a representative description of the plasma regimes possible in high-pressure air. These results show promise for the generation of plasma, as a radical pool, in high-pressure environments, for the enhancement of fuel oxidation chemistry.

IV. Conclusion

The architecture and operating principles of a novel (approximately 1000 USD), high-voltage nanosecond pulse generator intended for the generation of diffuse high-pressure plasma volumes in reactive gases is presented. The characteristics of the generator's output voltage and current, and the energy delivered to various resistive loads are reported. The energy per pulse of the discharge is calculated as a function of the pressure in the discharge cell, where a decreasing trend is observed. Diffuse plasma volumes can be sustained in air at 26 psig, at a pulse repetition frequency of 1 kHz, a peak voltage of 23 kV, and a deposited energy of 733 µJ/pulse. These results show promise for the implementation of non-equilibrium PAC at atmospheric pressure and above.

V. Acknowledgement

The authors would like to acknowledge Lou Cusmich and Gerald Lepkyj of McGill University, and Dr. Scott Pendleton for insightful and helpful discussions. M.D.G. Evans would like to acknowledge the financial support from the McGill Engineering Doctoral Award via the Tomlinson Doctoral Award, and the *Fonds de Recherche du Québec, Nature et Technologies* via the B2 doctoral award. The authors would like to acknowledge the support of Siemens Canada, the Natural Sciences and Engineering Research Council of Canada, and the *Fonds de Recherche du Québec, Nature et Technologies*.

VI. References

[1] N. A. Popov, "Kinetics of plasma-assisted combustion: effect of non-equilibrium excitation on the ignition and oxidation of combustible mixtures," *Plasma Sources Sci. Technol.*, vol. 25, no. 4, p. 43002, 2016.

[2] S. M. Starikovskaia, N. B. Anikin, S. V. Pancheshnyi, D. V. Zatsepin, and A. Y. Starikovskii, "Pulsed breakdown at high overvoltage: development, propagation and energy branching," *Plasma Sources Sci. Technol.*, vol. 10, no. 2, pp. 344–355, May 2001.

[3] D. Pai, G. D. Stancu, D. A. Lacoste, and C. O. Laux, "Nanosecond repetitively pulsed discharges in air at atmospheric pressure—the glow regime," *Plasma Sources Science and Technology*, vol. 19. p. 65015, 2010.

[4] T. Li, I. V. Adamovich, and J. A. Sutton, "Effects of non-equilibrium plasmas on low-pressure, premixed flames. Part 1: CH* chemiluminescence, temperature, and OH," *Combust. Flame*, vol. 165, pp. 50–67, 2015.

[5] Y. Ju and W. Sun, "Plasma assisted combustion: Dynamics and chemistry," *Prog. Energy Combust. Sci.*, vol. 48, pp. 21–83, 2015.

[6] M. A. Boumehdi, S. A. Stepanyan, P. Desgroux, G. Vanhove, and S. M. Starikovskaia, "Ignition of methane- and n-butane-containing mixtures at high pressures by pulsed nanosecond discharge," *Combust. Flame*, Dec. 2014.

[7] S. V. Pancheshnyi, D. A. Lacoste, A. Bourdon, and C. O. Laux, "Ignition of propane-air mixtures by a repetitively pulsed nanosecond discharge," *IEEE Trans. Plasma Sci.*, vol. 34, no. 6, pp. 2478–2487, 2006.

[8] M. S. Bak, S. K. Im, and M. Cappelli, "Nanosecond-pulsed discharge plasma splitting of carbon dioxide," *IEEE Trans. Plasma Sci.*, vol. 43, no. 4, pp. 1002–1007, 2015.

[9] Y. F. Yue, S. Mohades, M. Laroussi, and X. Lu, "Measurements of Plasma-Generated Hydroxyl and Hydrogen Peroxide Concentrations for Plasma Medicine Applications," *IEEE Trans. Plasma Sci.*, vol. accepted, pp. 1–5, 2016.

[10] A. Lin, B. Truong, A. Pappas, L. Kirifides, A. Oubarri, S. Chen, S. Lin, D. Dobrynin, G. Fridman, A. Fridman, N. Sang, and V. Miller, "Uniform Nanosecond Pulsed Dielectric Barrier Discharge Plasma Enhances Anti-Tumor Effects by Induction of Immunogenic Cell Death in Tumors and Stimulation of Macrophages," *Plasma Process. Polym.*, vol. 12, no. 12, pp. 1392–1399, 2015.

[11] V. M. Efanov, P. M. Yarin, A. V. Kricklenko, and V. A. Mankevich, "High voltage nanosecond pulsers for plasma chemistry and gas discharge," *Proc. 2008 IEEE Int. Power Modul. High Volt. Conf. PMHVC*, pp. 178–180, 2008.

[12] V. I. Brylevsky, V. M. Efanov, A. F. Kardo-Sysoev, and I. G. Tchashnicov, "Power Nanosecond Semiconductor Opening Plasma Switches," pp. 51–54, 1996.

[13] P. V. Vasil'ev, S. K. Lyubutin, M. S. Pedos, A. V Ponomarev, S. N. Rukin, B. G. Slovikovskii, S. P. Timoshenkov, and S. O. Cholakh, "A nanosecond SOS-generator with a 20-kHz pulse repetition rate," *Instruments Exp. Tech.*, vol. 53, no. 6, pp. 830–835, 2010.

[14] P. V. Vasil'ev, S. K. Lyubutin, M. S. Pedos, A. V. Ponomarev, S. N. Rukin, A. K. Sabitov, B. G. Slovikovskii, S. P. Timoshenkov, S. N. Tsyranov, and S. O. Cholakh, "A SOS-Generator for technological applications," *Instruments Exp. Tech.*, vol. 54, no. 1, pp. 54–60, 2011.

[15] J. M. Sanders, A. Kuthi, and M. A. Gundersen, "Optimization and implementation of a solid state high voltage pulse generator that produces fast rising nanosecond pulses," *IEEE Trans. Dielectr. Electr. Insul.*, vol. 18, no. 4, pp. 1228–1235, 2011.

[16] S. J. Pendleton, D. Singleton, A. Kuthi, and M. A. Gundersen, "Compact solid state high repetition rate variable amplitude pulse generator," *2009 IEEE Pulsed Power Conf.*, pp. 922–925, 2009.

[17] W. C. Nunnally, "Magnetic Switches and Circuits.," 1982.

[18] D. Zhang, Y. Zhou, J. Wang, and P. Yan, "A compact, high repetition-rate, nanosecond pulse generator based on magnetic pulse compression system," *IEEE Trans. Dielectr. Electr. Insul.*, vol. 18, no. 4, pp. 1151–1157, 2011.

[19] T. Shao, D. Zhang, Y. Yu, C. Zhang, J. Wang, P. Yan, and Y. Zhou, "A compact repetitive unipolar nanosecond-pulse gnerator for dielectric barrier discharge application," *IEEE Trans. Plasma Sci.*, vol. 38, no. 7, pp. 1651–1655, 2010.

[20] C. Zhang, T. Shao, R. Wang, Z. Zhou, Y. Zhou, and P. Yan, "A comparison between characteristics of atmospheric-pressure plasma jets sustained by nanosecond- and microsecond-pulse generators in helium," *Phys. Plasmas*, vol. 21, no. 10, p. 103505, 2014.

[21] M. Gundersen, A. Kuthi, P. Gabrielsson, and M. Behrendand, "Nanosecond pulse generator using a fast recovery diode," *Conf. Rec. Twenty-Sixth Int. Power Modul. Symp. 2004 2004 High-Voltage Work.*, pp. 603–606, 2004.

[22] I. V. Adamovich, W. R. Lempert, J. W. Rich, Y. G. Utkin, and M. Nishihara, "Repetitively Pulsed Nonequilibrium Plasmas for Magnetohydrodynamic Flow Control and Plasma-Assisted Combustion," *J. Propuls. Power*, vol. 24, no. 6, pp. 1198–1215, 2008.

[23] D. R. Singleton, A. Kuthi, J. M. Sanders, M. A. Gundersen, A. Simone, and S. J. Pendleton, "Low energy compact power modulators for transient plasma ignition," *IEEE Trans. Dielectr. Electr. Insul.*, vol. 18, no. 4, pp. 1084–1090, 2011.

[24] J. M. Bergthorson and M. J. Thomson, "A review of the combustion and emissions properties of advanced transportation biofuels and their impact on existing and future engines," *Renew. Sustain. Energy Rev.*, vol. 42, pp. 1393–1417, 2015.

[25] S. Nagaraja, T. Li, J. A. Sutton, I. V. Adamovich, and V. Yang, "Nanosecond plasma enhanced H 2 / O 2 / N 2 premixed flat flames," *Proc. Combust. Inst.*, vol. 35, no. 3, pp. 1–22, 2015.

[26] A. Y. Starikovskii, N. B. Anikin, I. N. Kosarev, E. I. Mintoussov, M. M. Nudnova, A. E. Rakitin, D. V. Roupassov, S. M. Starikovskaia, and V. P. Zhukov, "Nanosecond-Pulsed Discharges for Plasma-Assisted Combustion and Aerodynamics," *J. Propuls. Power*, vol. 24, no. 6, pp. 1182–1197, 2008.

[27] D. A. Lacoste, J. P. Moeck, D. Durox, C. O. Laux, and T. Schuller, "Effect of Nanosecond Repetitively Pulsed Discharges on the Dynamics of a Swirl-Stabilized Lean Premixed Flame," *Vol. 1A Combust. Fuels Emiss.*, p. V01AT04A054, 2013.

[28] G. Pilla, D. Galley, D. A. Lacoste, F. Lacas, D. Veynante, and C. O. Laux, "Stabilization of a Turbulent Premixed Flame Using a Nanosecond Repetitively Pulsed Plasma," *IEEE Trans. Plasma Sci.*, vol. 34, no. 6, pp. 2471–2477, Dec. 2006.

[29] D. Z. Pai, D. A. Lacoste, and C. O. Laux, "Nanosecond repetitively pulsed discharges in air at atmospheric pressure—the spark regime," *Plasma Sources Sci. Technol.*, vol. 19, no. 6, p. 65015, Dec. 2010.

[30] D. A. Lacoste, J. P. Moeck, C. O. Paschereit, and C. O. Laux, "Effect of Plasma Discharges on Nitric Oxide Emissions in a Premixed Flame," *J. Propuls. Power*, vol. 29, no. 3, pp. 748–751, May 2013.

[31] M. D. G. Evans, J. M. Bergthorson, and S. Coulombe, "High-voltage, high-frequency pulse generator for nonequilibrium plasma generation and combustion enhancement," *IEEE Trans. Plasma Sci.*, vol. doi, no. 10, p. 10.1109/TPS.2016.2606484, 2016.

[32] C. Guerra-Garcia, M. Martinez-Sanchez, R. B. Miles, and A. Starikovskiy, "Localized pulsed nanosecond discharges in a counterflow nonpremixed flame environment," *Plasma Sources Sci. Technol.*, vol. 24, no. 5, p. 55010, 2015.

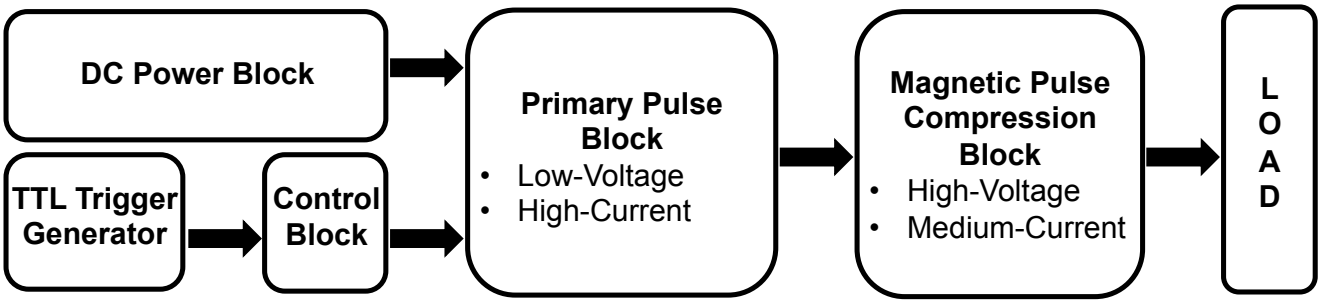

Fig. 1. Block diagram of the MPC generator.

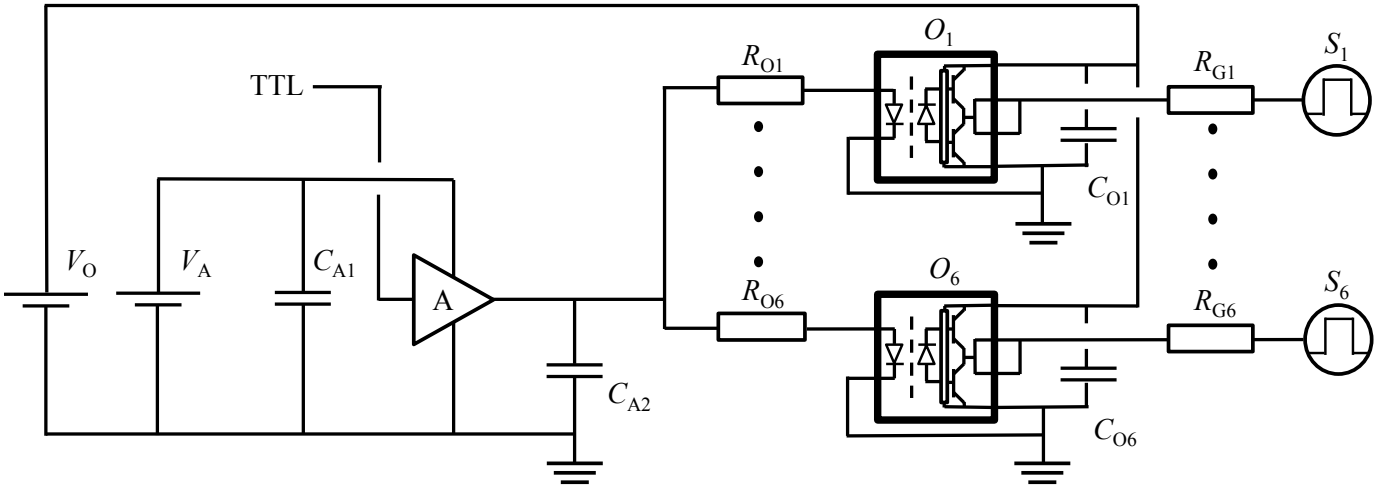

Fig. 2. Architecture of the Control Block Circuit.

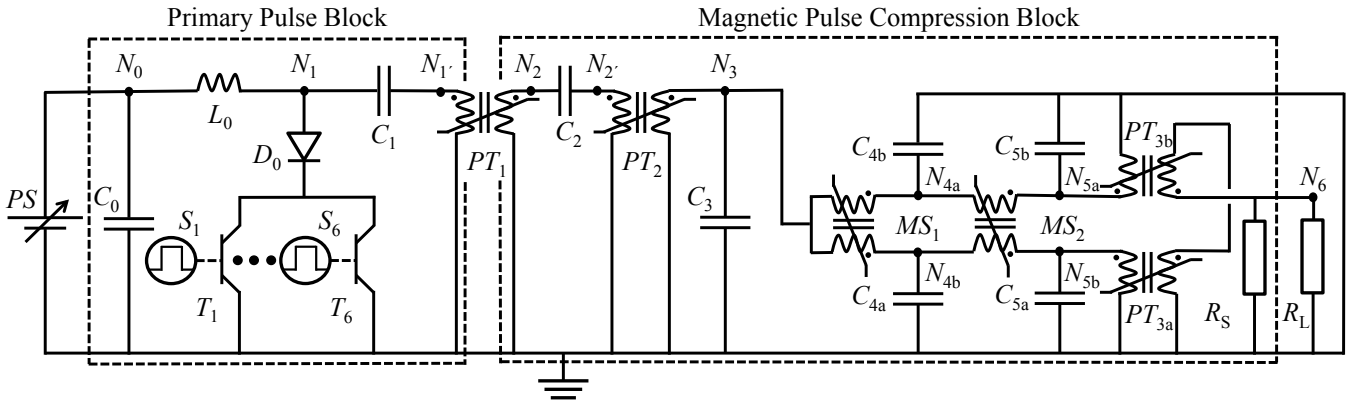

Fig. 3. Equivalent circuit of the combined Primary Pulse Block and the Magnetic Pulse Compression Block shown with the dashed outlines.

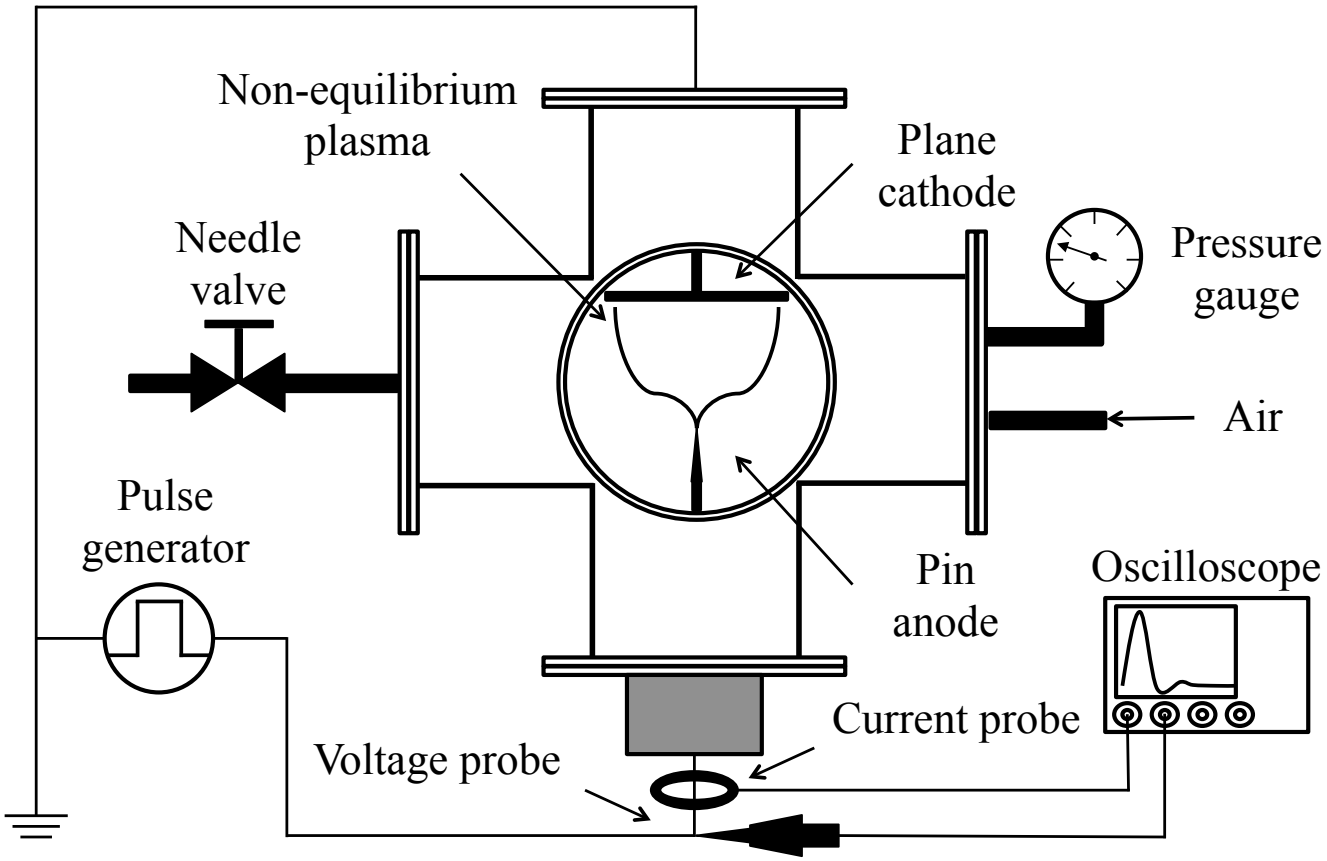

Fig. 4. Schematic of the high-pressure gas discharge cell with the schematic of the electrical diagnostics.

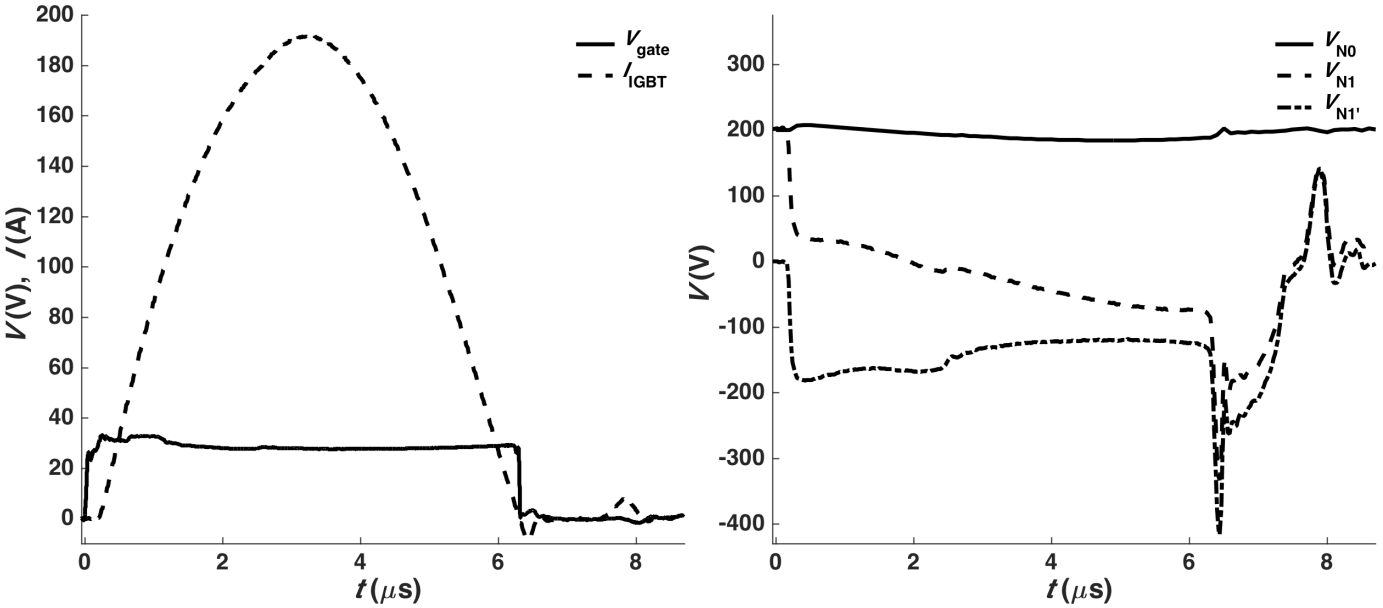

Fig. 5. Control signal, V_{gate}, and C_1 discharge current, I_{IGBT}, (left) and voltages at nodes N_0, N_1, and $N_{1'}$ (right).

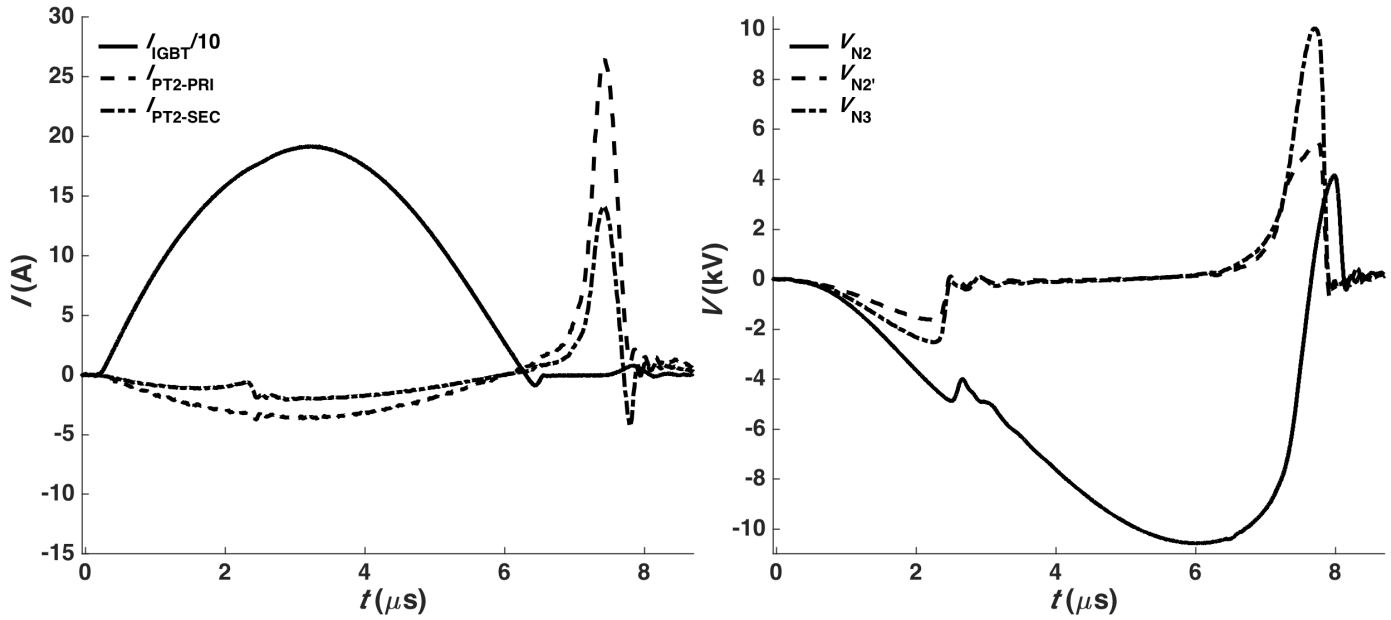

Fig. 6. Currents I_{IGBT}, $I_{PT2\text{-}PRI}$, and $I_{PT2\text{-}SEC}$ (left) and voltages at nodes N_{2a}, N_{2b}, and N_3 (right).

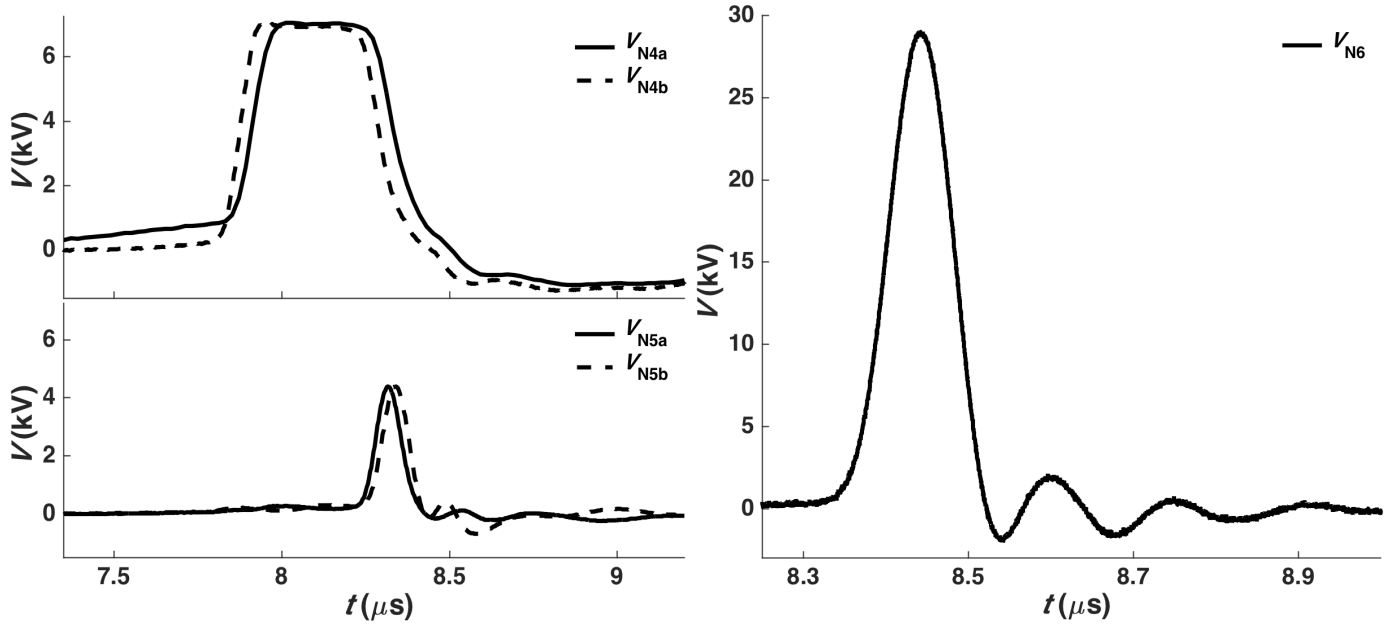

Fig. 7. Voltages in the branches of the series compression cell (left), and output voltage (right) of the generator into a 3 kΩ load.

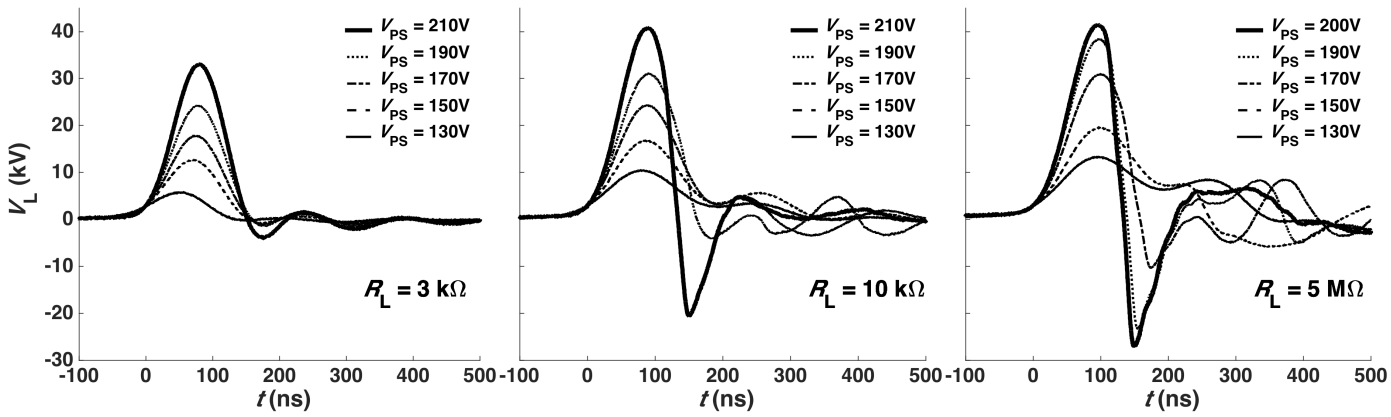

Fig. 8. Output voltage of the MPC generator across 3 kΩ (left), 10 kΩ (center), and 5 MΩ (right) loads.

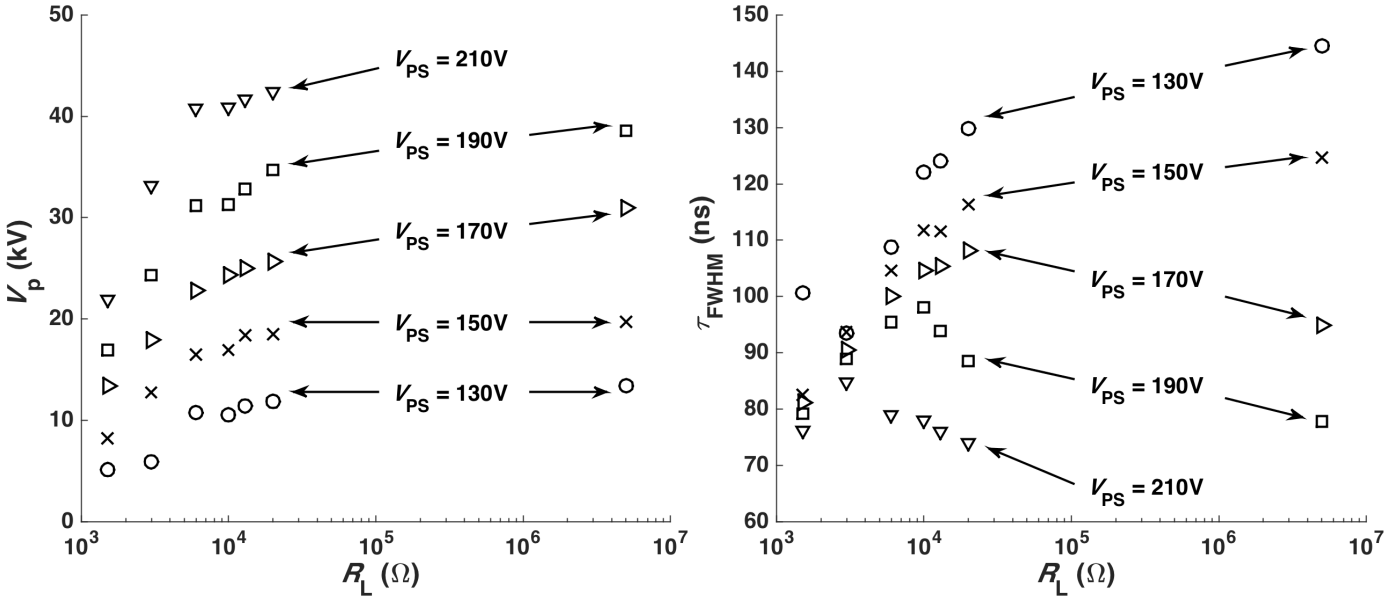

Fig. 9. Peak voltage, V_p, (left) and pulse width at FWHM, τ_{FWHM}, (right) as a function of the load impedance R_L, for various charging voltages of *PS*.

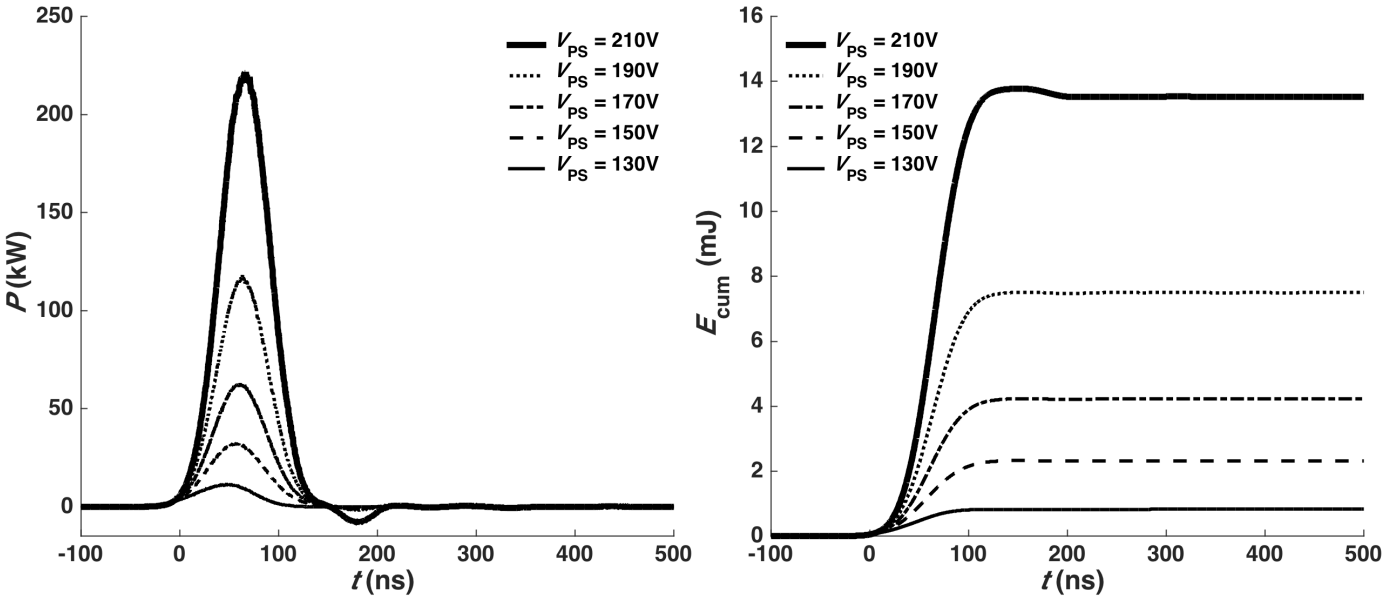

Fig. 10. Instantaneous power, P, (left), cumulative energy deposition, E_{cum}, (right) into a 3 kΩ load.

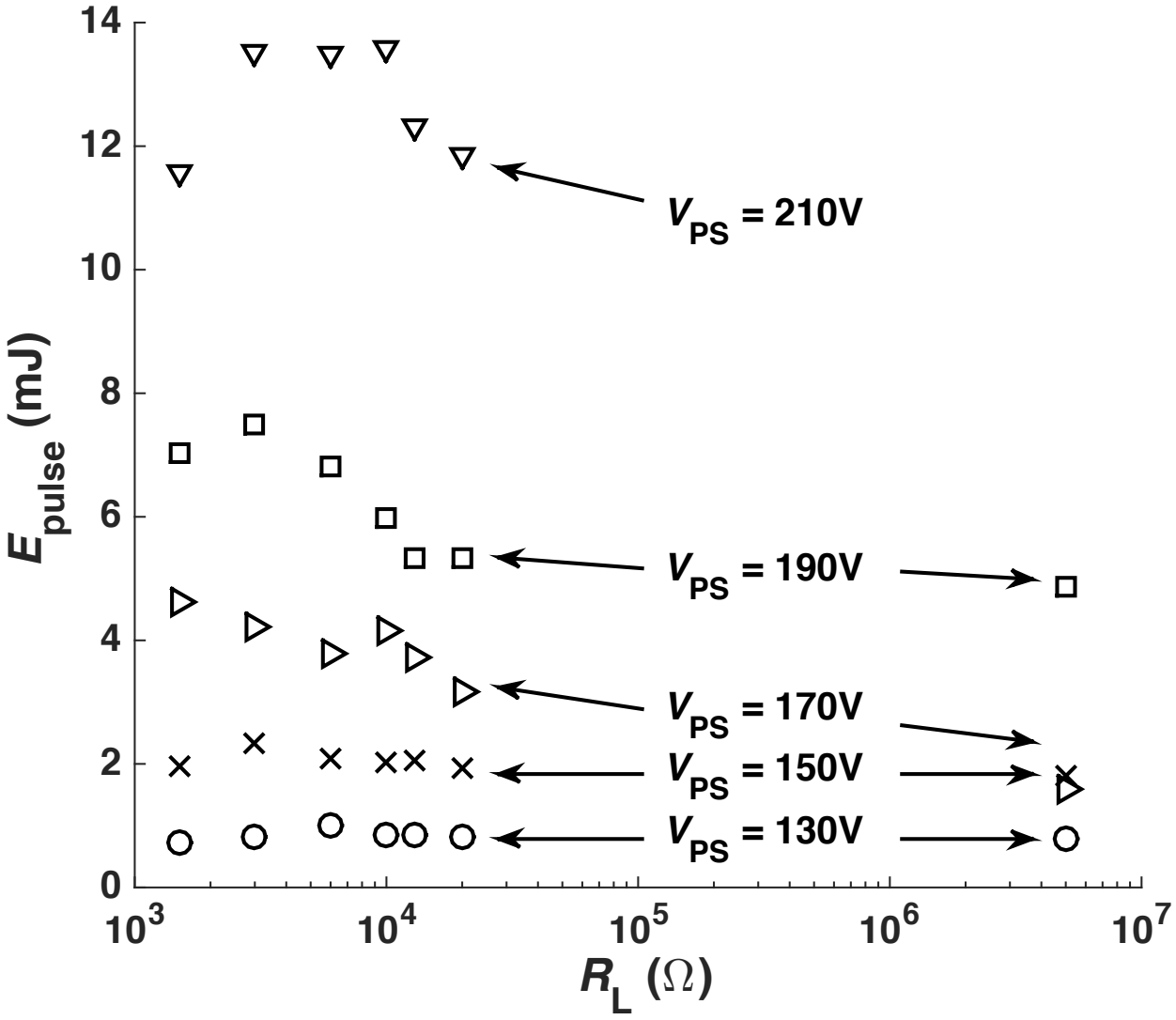

Fig. 11. Energy deposited per pulse, E_{pulse}, as a function of the load impedance, R_L, for various charging voltages provided by *PS*.

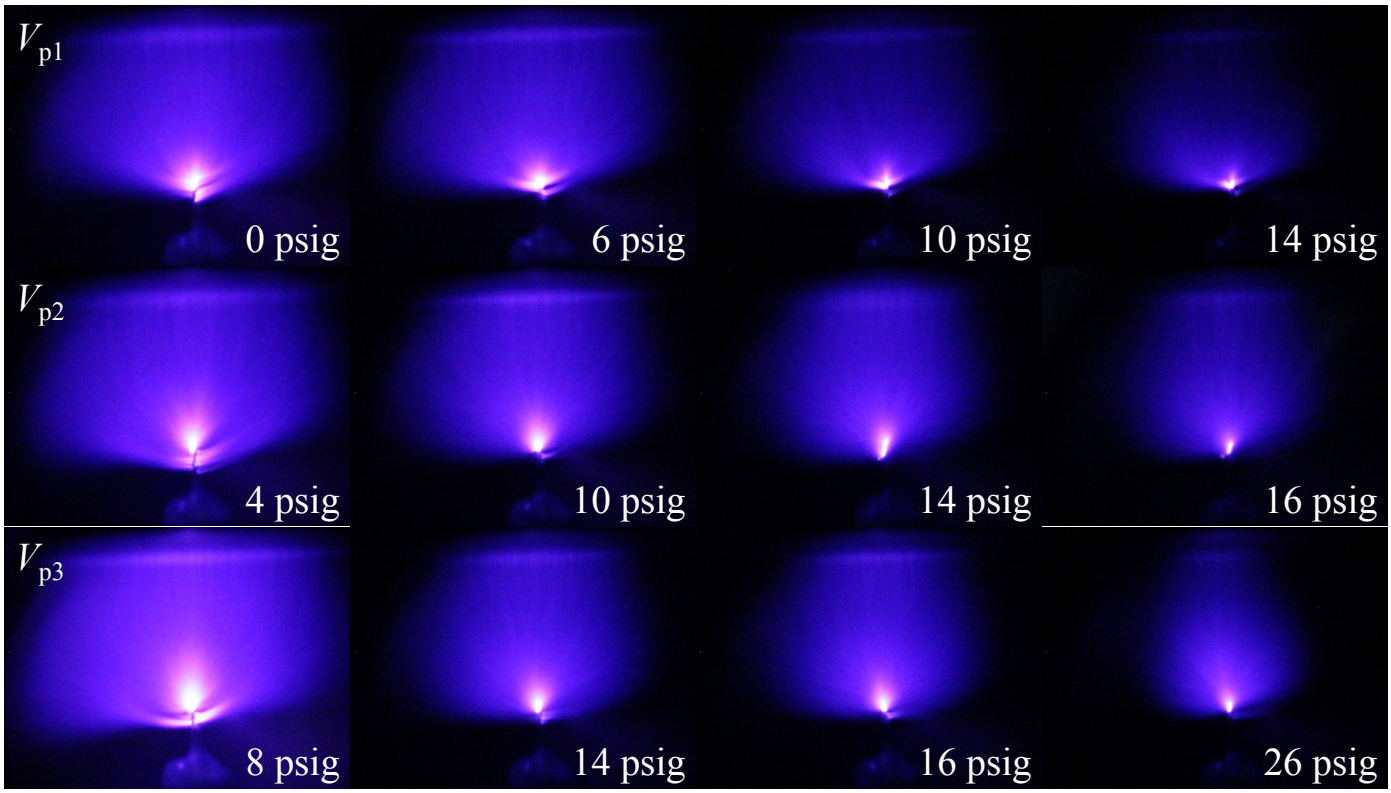

Fig. 12. Digital photographs of the diffuse plasma volumes formed in air at 1 kHz. Each row shows the evolution of the discharge volume with increasing pressure (left to right), for a given excitation waveform (V_{p1}, V_{p2}, and V_{p3}).

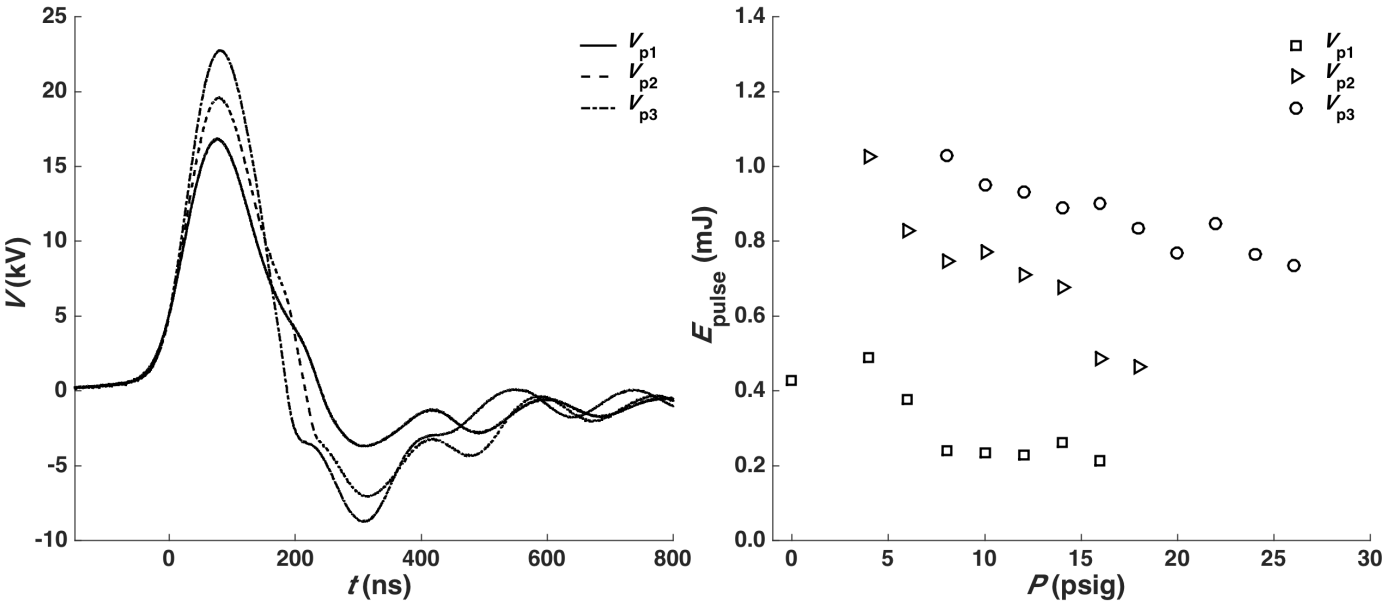

Fig. 13. Applied voltage pulses at the glow limit (left) and the energy deposited per pulse (right).